The protective role of hydrozincite during initial corrosion of a Cu40Zn alloy in chloride-containing laboratory atmosphere

Xian Zhang, Xiaoyan Liu, Inger Odnevall Wallinder, Christofer Leygraf*

KTH Royal Institute of Technology, Div. Surface and Corrosion Science, School of Chemical Science and Engineering, Dr. Kristinas v. 51, SE-100 44 Stockholm, Sweden

ABSTRACT

Hydrozincite, $Zn_5(CO_3)_2(OH)_6$, was recently found to play a key role in reducing corrosion product flaking on Cu–Zn alloys. A fundamental study was undertaken to explore the underlying mechanisms, in particular why hydrozincite can suppress the interaction between chlorides and the alloy surface. Hydrozincite could be formed by exposure of Cu40Zn to air at 70% relative humidity and 1000 ppm of CO_2 resulting in a surface of decreased wettability. Its presence reduces the initial spreading ability of NaCl-containing droplets and lowers the overall initial corrosion rate when the alloy is exposed to pre-deposited NaCl and wet/dry cycles.

© 2015 The Authors. Published by Elsevier Ltd. This is an open access article under the CC BY license (http://creativecommons.org/licenses/by/4.0/).

1. Introduction

Copper and copper alloys form a large group of important materials for constructional and industrial applications, with characteristic features ranging from mechanical and physical properties, over visual appearance to high corrosion resistance in a broad range of liquid and atmospheric environments. Brass is a copper-alloy family primarily consisting of copper and zinc that exhibit good strength and ductility. Based on the proportions between zinc and copper the brasses can be further classified into subgroups with different properties [1]. α-brass with up to approximately 35 wt% zinc consists of only one phase with face-centered cubic crystal structure. α/β-brass (also called duplex brass) consists of 35–45 wt% zinc and contains α-phase dendrites with a β-phase, having a body-centered cubic structure, surrounding the dendrites [2].

Extensive investigations have been performed concerning the atmospheric corrosion of copper and copper alloys in chloride-containing field or laboratory atmospheres. Cuprite (Cu_2O) seems always to be the initial phase in the evolution of the copper patina. The subsequent formation of nantokite (CuCl) results from the interaction of the cuprite surface with chlorides with the subsequent transformation to atacamite or its isomorphous phase paratacamite ($Cu_2Cl(OH)_3$) as the end corrosion products [3–5]. The same constituents have also been identified within the patina after exposure in laboratory conditions with humidified air and pre-deposited NaCl [6,7]. When brass containing 15 wt% Zn (Cu15Zn) was exposed in chloride-rich atmospheres [4,8,9], additional zinc-containing corrosion products, mainly amorphous zinc hydroxycarbonate, hydrozincite ($Zn_5(CO_3)_2(OH)_6$) and zinc oxide (ZnO), were observed within the patina.

The starting point for this investigation is based on a previously reported study [4,9] on the corrosion properties of copper and commercial copper-based alloys used in outdoor building applications during long-term exposures in marine atmospheric environments. It was found that the single phase Cu15Zn alloy exhibits lower tendency for corrosion product flaking than bare Cu and a bronze (Cu4Sn) alloy in chloride containing atmospheres [4,9]. This was attributed to the early formation of zinc hydroxycarbonate, $Zn_5(CO_3)_2(OH)_6$, which hinders the formation of nantokite, CuCl, a precursor of atacamite $Cu_2Cl(OH)_3$. The flaking process was attributed to an observed volume expansion during transformation of CuCl to $Cu_2Cl(OH)_3$.

Although the protective nature of zinc hydroxycarbonate on zinc has been thoroughly investigated by Muster et al., and explained by, e.g., surface charge and surface wetting effects [10], it was decided to undertake a fundamental study of the possible cause of the beneficial effect of hydrozincite under exposure conditions which are

* Corresponding author. Fax: +46 8 208284.
E-mail address: chrisl@kth.se (C. Leygraf).

as similar as possible with those of the mechanistic flaking study mentioned above [4,9]. For this purpose a brass alloy (Cu40Zn) was chosen with a high Zn-content (40 wt%) in order to facilitate the formation of hydrozincite. This study includes both diamond polished Cu40Zn and Cu40Zn with pre-formed hydrozincite that have been exposed to a chloride containing laboratory environment through pre-deposition of NaCl followed by cyclic wet/dry humidity exposures. Another reason for chosing the dual-phase Cu40Zn alloy was the possibility to explore the influence of microstructure on corrosion initiation. The wetting characteristics and surface roughness of the differently prepared surfaces were compared. The initial evolution of corrosion products was then followed with a series of complementary analytical techniques, which include in situ infrared reflection absorption spectroscopy (in situ IRAS), light optical microscopy (LOM), scanning electron microscopy with X-ray microanalysis (SEM/EDS) and confocal Raman spectroscopy (CRM). This combination of analytical techniques permits a relative comparison to be made of the formation rate of corrosion products on Cu40Zn with and without pre-formed hydrozincite and exposed to a chloride containing atmospheric environment, in order to possibly establish the corrosion protective role of hydrozincite under conditions which are similar to those during the corrosion product flaking study.

2. Material and methods

2.1. Materials and surface preparation

A commercial Cu40Zn alloy (60 wt% Cu and 40 wt% Zn) was kindly provided by Aurubis Finland Oy. The chemical bulk composition in wt-%, based on EDS-analysis, is given in Table 1. Cu40Zn samples were cut to a dimension of 1×1 cm or 2×2 cm for microstructure characterization and wet/dry cyclic exposure. Each sample was mechanically wet ground down to 2400 grit and then diamond polished successively down to 0.25 μm. Prior to the experiments, all the samples were ultrasonically cleaned in analytical grade ethanol for 10 min and subsequently dried by cold nitrogen gas prior to storing in a desiccator overnight.

Bare copper (99.98% Cu) and bare zinc (0.2% Cu, 0.07% Ti) were prepared as described above and investigated for comparison.

2.2. Laboratory wet/dry cycle exposure conditions

Parallel experiments were conducted in two ways: by exposures in a climatic chamber and by exposures in a chamber for in situ IRAS (Infrared reflection absorption spectroscopy) measurements. Wet/dry cycle experiments were carried out on Cu40Zn samples with pre-deposited NaCl (4 or 0.1 μg cm^{-2}) and then exposed to the following cyclic exposure conditions: the first cycle 4 h (RH 90%) and 2 h (RH 0%), the second cycle 16 h (RH 90%) and 2 h (RH 0%). These cycles were repeated several times, with more detailed information on the wet/dry cyclic exposure given elsewhere [11].

NaCl (in a saturated 99.5% ethanol solution) was pre-deposited onto the surfaces by means of a transfer pipette. NaCl crystals were relatively homogeneously distributed over the surface upon ethanol evaporation. The amount of NaCl particles was weighed by a microbalance (Mettler Toledo Excellence) and normalized to the geometric surface area of the samples. Detailed information on the procedure for NaCl pre-deposition is given elsewhere [12].

Exposures in the climatic chamber were employed by means of a WEISS WK1000 climatic chamber. Samples with pre-deposited NaCl were attached on Plexiglas fixtures and exposed 45° from the horizontal in the chamber. The exposure of all samples started simultaneously following the wet/dry cycles described above. Each Plexiglas fixture was withdrawn after 1, 2, 6 and 14 cycles (corresponding to 6 h, 1, 3, 7 days).

Exposures during in situ IRAS measurements were performed in a chamber inside the infrared spectrometer with humidified air following the same wet/dry cycles as above. By mixing dry and wet pre-cleaned compressed air of reduced CO$_2$ (lower than 20 ppm), controlled air humidity conditions were obtained. A small flow of air with 1.17% CO$_2$ from a CO$_2$ cylinder was added into the humidity chamber to obtain ambient CO$_2$ concentration, 350 ± 50 ppm. To accelerate the formation of hydrozincite, Cu40Zn samples were pre-exposed to the humidity chamber at 70% RH and with a flow of 1000 ± 200 ppm CO$_2$. Abbreviations defined to distinguish the different samples are displayed in Table 2. Experimental details are given elsewhere [13].

2.3. Surface and patina analysis

2.3.1. SEM/EDS (Scanning electron microscopy and energy dispersive spectroscopy)

Measurements were carried out to obtain morphology and elemental information from corrosion products formed. Surface analysis was conducted be means of a FEI-XL 30 Series instrument, equipped with an EDS system (EDAX Phoenix) with an ultra-thin windows Si–Li detector and with another EDS system: X-Max SDD (Silicon Drift Detector) 20 mm^2 detector (Oxford Instruments). All surface images (75% SE, secondary electrons and 25% BSE, backscattered electrons) were obtained with an accelerating voltage of 20 kV.

2.3.2. SKPFM (Scanning Kelvin probe force microscopy)

Analysis was conducted to determine the surface topography and Volta potential mappings simultaneously on the same surface area, by using a Nanoscope IV AFM with facilities for Volta potential measurements in two-pass mode. The probe was PtIr-coated Si (Bruker, Germany) with a nominal spring constant of 1–5 N m^{-1} and a resonance frequency of 60–100 kHz.

2.3.3. XPS (X-ray photoelectron spectroscopy)

Measurements were performed to obtain compositional information of the surface region of corrosion products. XPS spectra were recorded at different positions using a Kratos AXIS UltraDLD X-ray photoelectron spectrometer (Kratos Analytical, Manchester, UK) with a monochromatic Al X-ray source operating at 150 W. Detailed scans of Cu 2p, Zn 2p, O 1s and C 1s were recorded at high resolution (20 eV) using the C 1s peak at 285.0 eV for charge-shift corrections.

2.3.4. AFM (Atomic force microscope)

Analysis was employed to obtain the surface topography, by means of a Nanoscope Multimode 8 AFM (Bruker, Germany operating in air and using tapping mode. For these measurements a triangular silicon nitride cantilever having a tip radius of about 8 nm (TESPA) was used.

Table 1
EDS analysis of the Cu40Zn alloy.

Cu (wt%)	Zn (wt%)	Others, mainly S and Pb (wt%)
60 ± 0.2	40 ± 0.2	<0.3

Table 2
Abbreviations defined for pre-treated Cu40Zn samples.

Abbreviation	Condition
DP	Diamond polished and stored in a desiccator overnight
HZ3	Pre-exposed to 70% RH and 1000 ppm CO$_2$ for 3 days
HZ7	Pre-exposed to 70% RH and 1000 ppm CO$_2$ for 7 days

2.3.5. Contact angle measurements

Measurements were performed to examine the surface wettability by utilizing a PGX instrument (FIBRO System AB, Sweden). The water droplet is illuminated when dispensed on the surface and its shape is immediately captured by a high resolution CCD camera. The image is examined and the contact angle is determined using the average value of 10 measurements.

2.3.6. IRAS (Infrared reflection absorption spectroscopy)

Near-surface analysis was performed to identify functional groups in the corrosion products by means of a commercial Digi-lab 4.0 Pro FTIR (Fourier transform infrared reflection spectroscopy) spectrometer with a MCT detector (4000–400 cm^{-1}). In situ spectra were recorded during the dry part of any cycle by acquiring 1024 scans with a resolution of 4 cm^{-1} for each spectrum. The results are presented in absorbance units ($-\log(R/R_0)$), where R is the reflectance of the exposed sample surface and R_0 the reflectance of the non-exposed sample [14]. A freshly polished and aged Cu40Zn surface was used for the background corrections.

2.3.7. CRM (Confocal Raman microspectroscopy)

Measurements were employed to display the lateral distribution of functional groups within the corrosion products by utilizing a WITec alpha300 system equipped with a laser source of wavelength 532 nm. Measurements were obtained with a Nikon objective 100, Nikon NA0.9 NGC, together with a pinhole of 100 μm diameter. The Raman spectra were generated in the scanned area with lateral and depth resolutions of approximately 300 nm and 2 μm, respectively.

2.3.8. LOM (Light optical microscopy)

Measurements were performed to investigate the surface morphological change under low magnification (50×–1000×) using a Leica DM 2700 M microscope with white light LED illumination.

3. Results and discussion

We start by characterizing the unexposed Cu40Zn surface and continue the characterization after formation of a more or less well developed hydrozincite layer atop of the Cu40Zn surface. A comparison is then made of the wetting characteristics, surface roughness and chemical composition, spreading of NaCl-droplets, corrosion rates and corrosion product distribution between the Cu40Zn surface without and with the preformed hydrozincite layer.

3.1. Microstructure characteristics on unexposed Cu40Zn

Before pre-forming hydrozincite, the diamond polished Cu40Zn alloy surface was analyzed by means of LOM to gain metallographic information, SEM/EDS for morphology and elemental compositional analyses, XPS for outermost surface oxide characterization and SKPFM to assess the surface topography and to map differences in Volta potential over the surface.

The microstructure of the diamond-polished Cu40Zn surface is shown in Fig. 1a, as viewed by LOM. The dual-phase structure of Cu40Zn is the result of solidification processes during casting [15] and evolves through precipitation of irregular shaped β-phase areas, typically sized from 5 to 20 μm, in the α-phase matrix [15,16]. To better reveal the alloy microstructure with β-phase grains in an α-phase matrix, a SEM image of the etched surface is displayed in Fig. 1b. The β-phase exhibits a granular-type morphology and occurs with an estimated surface coverage of approximately 10%. Elemental compositional EDS analysis of grains displayed in Fig. 1b and of several other grains are summarized in Table 3. They reveal a more zinc-rich β-phase (Zn/(Zn+Cu) mass ratio in the range of 42–46%) compared with the α-phase (Zn/(Zn+Cu) mass ratio in the range of 37–41%). During the cooling

Table 3
EDS analysis of the Cu/(Cu+Zn) and Zn/(Cu+Zn)-ratios (wt%) of individual α- and β-grains seen in Fig. 1.

Grain number	Cu/(Cu+Zn)	Zn/(Cu+Zn)
1 (α-phase)	60	40
2 (α-phase)	61	39
3 (β-phase)	54	46
4 (β-phase)	56	44
Interval of several (>5) observations (α-phase)	59–63	37–41
Interval of several (>5) observations (β-phase)	54–58	42–46

process the α-phase solidifies first and obtains a higher Cu-content, compared with the subsequent solidification of the β-phase of lower Cu-content [17]. The SEM/EDS investigation revealed further the presence of granular sulfur-rich inclusions, Fig. 1a (0.9% wt-% S, defined as S/(S+Cu+Zn)). Inclusions with a high content of sulfur were associated with a higher content of zinc compared with adjacent surface areas, and suggest a chemical composition similar to ZnS [17].

Compositional area analyses by means of XPS on the diamond-polished Cu40Zn surface (including both the α- and the β-phase) revealed a predominant copper-rich (70 ± 1 wt% Cu/(Zn + Cu)) outermost surface oxide. The calculated mass ratio denotes copper in oxidation state of (0) and (I) (binding energy 932.6 ± 0.1 eV) and zinc in oxidation state (II) at 1021.7 ± 0.1 eV. These peak positions suggest the presence of Cu_2O (cuprite) and ZnO (zincite)/$Zn(OH)_2$. The same compounds were also suggested in the IRAS investigation, see below.

Complementary measurements by SKPFM were performed on the diamond-polished surface with observed variations in topography and Volta potential as displayed in Fig. 2. The AFM-image (Fig. 2a) shows that the β-phase exhibits a slightly lower height than the α-phase, which may be a consequence of the polishing process. The β-phase exhibits a lower Volta potential compared with the surrounding α-phase, as revealed by the corresponding SKPFM-image (Fig. 2b). This suggests a lower relative nobility of the more zinc-rich β-phase with possibly a higher susceptibility for initial corrosion initiation. Furthermore, a granular area of circular shape of even lower Volta potential than both the α- and the β-phases was observed with SKPFM (Fig. 2b). This area most likely corresponds to zinc-enriched sulfur inclusions as seen in Fig. 1a. Their size and composition is consistent with previous findings for brass alloys [8,18,19].

To summarize, the diamond polished Cu40Zn alloy surface mainly consists of a smaller area fraction of the β-phase, locally distributed over the material that is slightly enriched in Zn and has a lower Volta potential than the surrounding α-matrix. The outermost surface oxide consists predominantly of cuprite (approx. 70 mass-%) and zinc-rich oxides/hydroxides.

3.2. Surface chemistry properties of preformed hydrozincite on Cu40Zn

We next turn our focus on the pre-formation of hydrozincite on Cu40Zn, in order to explore the effect of this corrosion product on the initial chloride-induced atmospheric corrosion of Cu40Zn. Since hydrozincite is known to form spontaneously in natural outdoor exposure conditions, several efforts were made to stimulate the formation of hydrozincite by exposing Cu40Zn in the laboratory to ambient or increased levels of CO_2 in humidified air. Finally, the reproducible formation of hydrozincite was accomplished by introducing around 1000 ppm of CO_2 for several days at 70% relative humidity. The confirmation of hydrozincite by IRAS and XPS is shown next, together with comparisons of surface wettability properties of Cu, Zn and Cu40Zn with or without pre-formed hydrozincite by means of contact angle measurements, and sur-
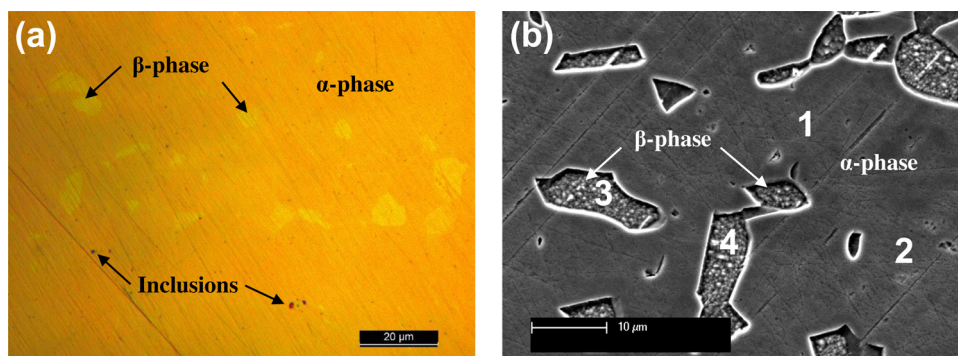
Fig. 1. Images showing the microstructure of the unexposed diamond polished Cu40Zn surface by means of LOM (a), and by SEM after slight etching (2 M HCl + 0.2 M FeCl$_3$) for 15 s (b).
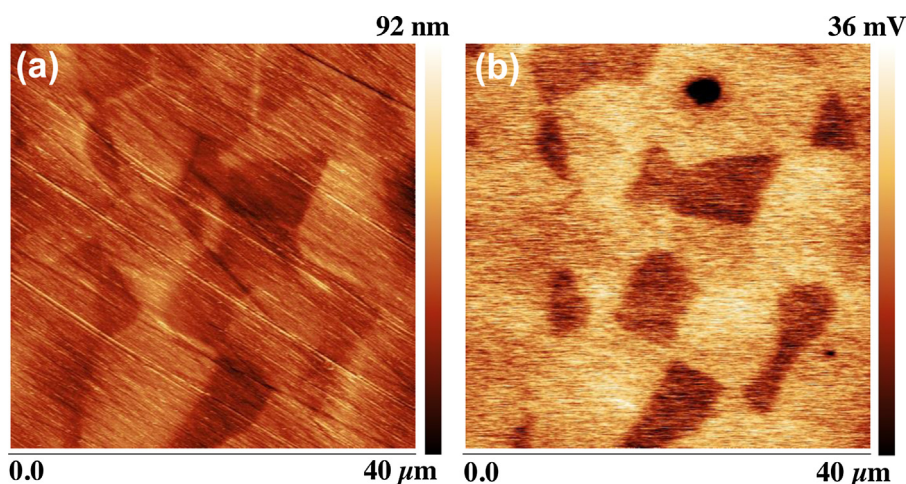

Fig. 2. AFM-based topography (a) and Volta potential mapping (b) obtained with SKPFM of an unexposed diamond polished Cu40Zn surface.

face topography comparisons based on AFM. As further described in Table 2, the samples are labelled DP, HZ3 and HZ7.

Fig. 3a displays the IRAS spectra obtained of the Cu40Zn sample labelled HZ3. Different functional groups were identified, all indicated by arrows in the figure. Starting from lower wavenumber and going upwards the peak at 478 cm^{-1} is attributed to zinc-oxygen vibrations in ZnO (zincite) [20] and the peak at 658 cm^{-1} from copper–oxygen vibrations in Cu$_2$O (cuprite) [7]. The bands in the region between 700 and 1100 cm^{-1} are assigned to Zn—O—H vibrations. The clearly resolved broad band from 1300 to 1600 cm^{-1} with two main peaks located at 1406 and 1508 cm^{-1} originate from anti-symmetric stretching modes of carbonate (CO$_3{}^{2-}$) [20]. Another peak also in this band located at 1590 cm^{-1} originates from vibrational modes of water. At higher wavenumber a broad band is seen ranging from 3200 to 3600 cm^{-1} which is commonly attributed to the presence of hydroxide ions (OH$^-$) or water. In all, the IRAS results suggest that the near-surface region of HZ3 consists of zincite and cuprite as surface constituents, and at least one more compound which contains hydroxide ions and carbonate ions, most likely hydrozincite [20] (zinc hydroxycarbonate, Zn$_5$ (CO$_3$)$_2$(OH)$_6$).

The IRAS-data, however, cannot unambiguously confirm if these ions are associated with Cu or with Zn. Therefore XPS was used to obtain complementary information of the surface composition of the samples labelled DP, HZ3 and HZ7. Fig. 3b shows the average mass ratio of the metal 2p$_{3/2}$-peaks originating from Cu(0,I, i.e., oxidation state 0 and I) with binding energy at 932.6 ± 0.1 eV and from Zn(II) with binding energy at 1021.9 ± 0.1 eV. No Cu(II) was detected. XPS confirmed the formation of carbonate (290 ± 0.1 eV) on the surface on HZ3 and HZ7. Observed peak positions of Zn 2p,

O 1s, and C 1s coincide with literature findings for hydrozincite [21]. It is evident that the mass ratio Cu/(Cu+Zn) decreases after exposure in humidified air and 1000 ppm of CO$_2$. This, together with an increased (CO$_3{}^{2-}$)/Zn-ratio, also seen with XPS, shows that the carbonate ion binds to Zn rather than to Cu. Furthermore, copper hydroxycarbonates are not abundant patina constituents on either copper or copper-based alloys at atmospheric conditions [3]. Together with the presented IRAS this forms evidence of formation of hydrozincite.

In all, 7 days of exposure of diamond polished Cu40Zn to humidified air at 70% relative humidity with addition of 1000 ppm of CO$_2$ results in a surface region which consists of hydrozincite and of cuprite and zincite to different extent.

Fig. 4 shows the change in contact angle of water droplets (~1 μL) on diamond polished Cu40Zn (DP) and on Cu40Zn surfaces with pre-formed hydrozincite following 3 and 7 days of exposure, HZ3 and HZ7. The contact angle increases as DP < HZ3 < HZ7, and it is evident that formation of hydrozincite results in a significantly more hydrophobic surface compared to the diamond polished surface. However, the surface wettability not only depends on the actual surface chemistry but also on surface roughness properties as well as the extent of surface contamination [10,22] whereby a smoother surface could result in better wetting properties than a rougher surface. Hence, the surface topography of the three Cu40Zn surfaces was evaluated by AFM, as displayed in Fig. 5, and increases as DP < HZ3 < HZ7. To separate the effect of surface roughness and wettability, contact angle and AFM measurements were also performed on bare Cu and bare Zn with the same surface treatments as Cu40Zn, i.e., diamond polished, 3 days in 70% relative humid-
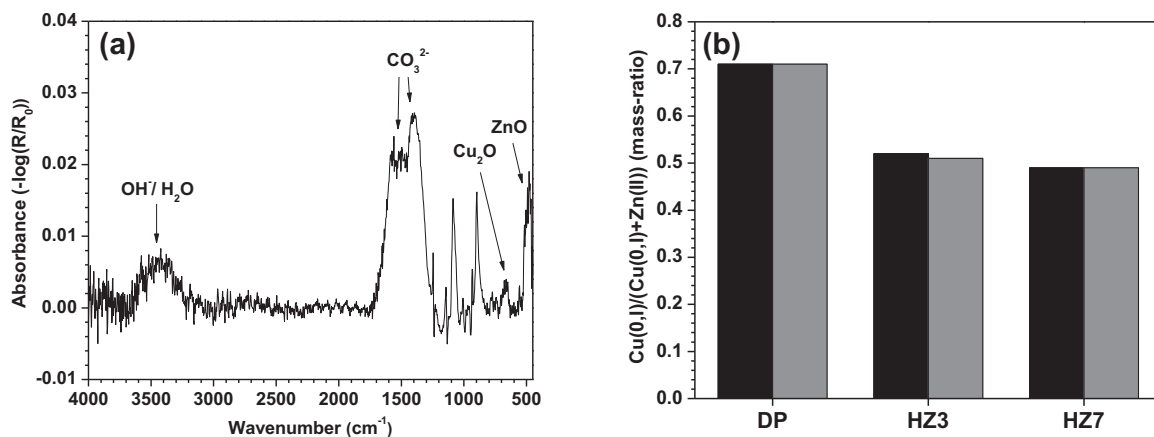
Fig. 3. (a) In situ IRAS spectrum obtained on Cu40Zn after 3 days in humidified air with 1000 ppm CO_2 (HZ3); (b) Average mass ratio of Cu(0,I)/(Cu(0,I)+Zn(II)) based on XPS measurements of two separate areas on three Cu40Zn samples, labelled DP, HZ3 and HZ7.
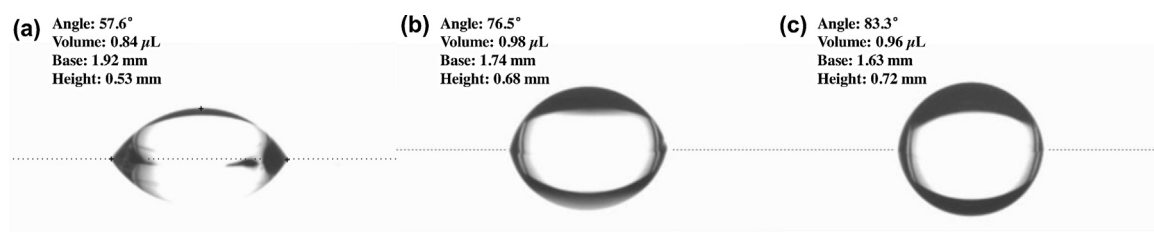

Fig. 4. The change in contact angle of water droplets illustrating the surface wettability of Cu40Zn: DP (a), HZ3 (b) and HZ7 (c).
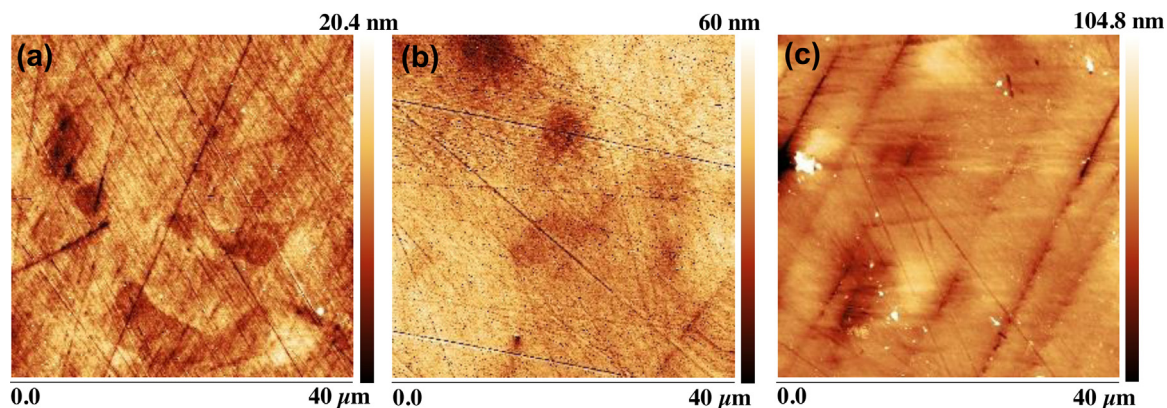

Fig. 5. AFM images showing surface topography of Cu40Zn: DP (a), HZ3 (b) and HZ7 (c).
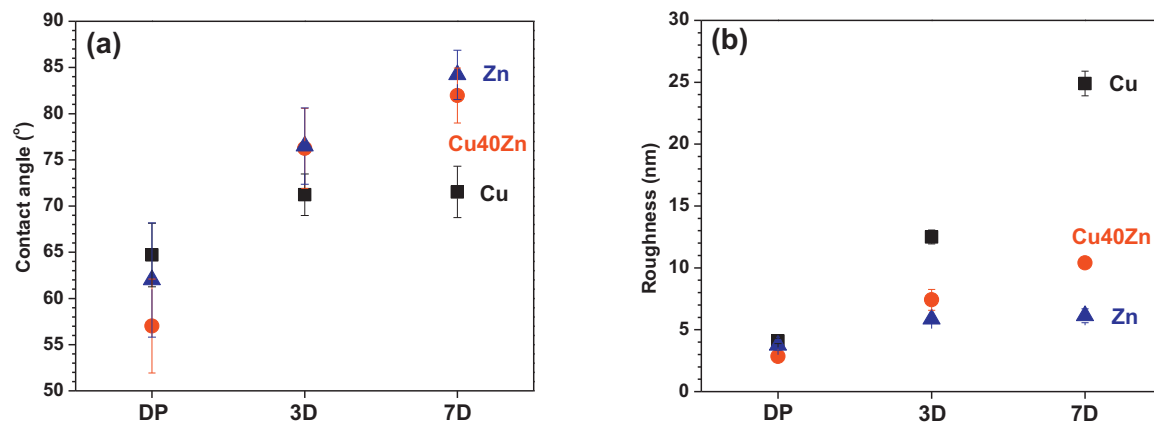

Fig. 6. The change in contact angle (a) and surface roughness (AFM) (b) on diamond polished (DP) and pre-treated Cu, Cu40Zn and Zn surfaces during 3 (3D) and 7 (7D) days, respectively. The error bars in the contact angle measurements are based on 10 independent measurements for each sample, and the error bars for surface roughness measurements on 2 independent measurements.
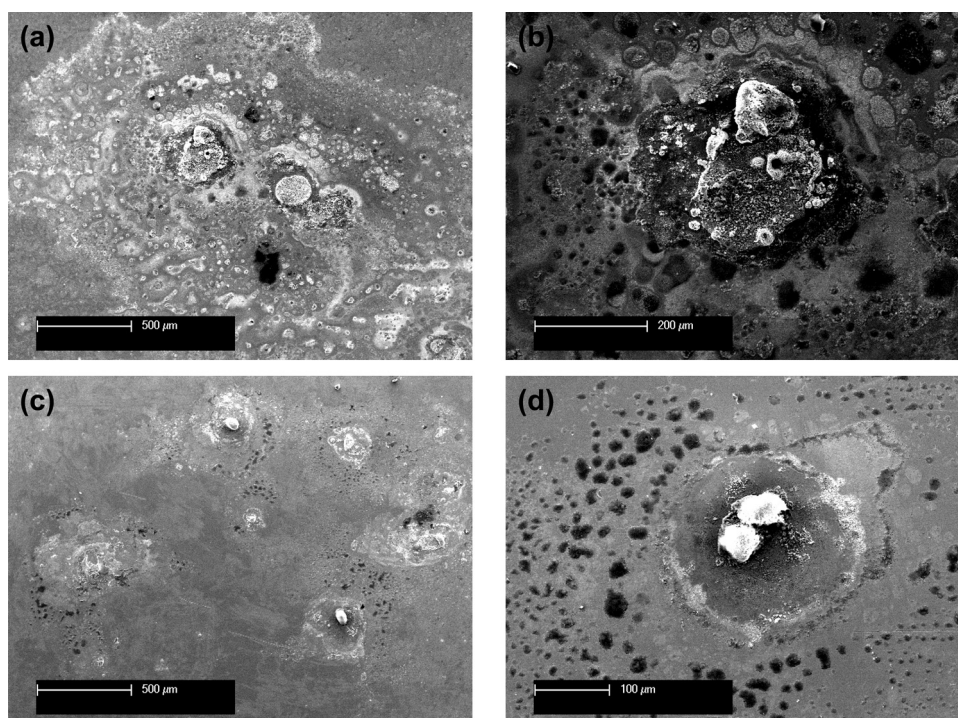
Fig. 7. SEM images of corrosion products formed on Cu40Zn, with and without pre-formed hydrozincite, (DP (a–b), HZ7 (c–d)) after 6 wet/dry cycles with pre-deposited NaCl ($4\,\mu g\,cm^{-2}$).

ity and 1000 ppm CO_2, and 7 days in the same environment. IRAS detected cuprite and hydrozincite as the main surface compounds on Cu and Zn respectively. The results are summarized in Fig. 6. The trend for bare Zn is quite similar to Cu40Zn, i.e., both contact angle and surface roughness increase with the extent of hydrozincite formation. For bare Cu, on the other hand, the contact angle increases only little while the surface roughness increases significantly with exposure in humidified air to which CO_2 has been added. This shows that increased surface roughness alone under current conditions does not result in any enhanced wettability. No large differences in surface contamination, derived from cleaning solvents and adventitious carbon (C 1s at 285.0 eV), were observed using XPS that could explain observed differences in wetting properties of the diamond-polished and pre-treated Cu40Zn samples. The overall conclusion is that the increased extent of hydrozincite formation on Cu40Zn and on bare Zn is the main reason for the decreased surface wettability.

3.3. Influence of hydrozincite on corrosion product formation

In an effort to explore the actual role of hydrozincite under initial chloride-induced atmospheric exposure conditions, Cu40Zn surfaces, diamond polished (DP) or with pre-formed hydrozincite (HZ7), were subject to pre-deposition of $4\,\mu g\,cm^{-2}$ NaCl and subsequent exposure to wet/dry cycles. The corrosion product formation was then compared with respect to morphology and elemental compositional (SEM/EDS) and near-surface chemical composition (IRAS).

After exposure to 6 wet/dry cycles, the corrosion product morphology of Cu40Zn with pre-formed hydrozincite (HZ7, Figs. 7a,b) is largely different from the diamond polished Cu40Zn without pre-deposited hydrozincite (DP, Figs. 7c,d). The corrosion products on HZ7 are seen as locally formed smaller islands, whereas on DP the corrosion products form much larger features. This difference is explained by differences in initial surface wetting properties as shown in the previous section. Upon deliquescence, the NaCl-droplets initially tend to retain as discrete droplets on HZ7 to a

much larger extent than on DP, where the droplets spread out more to form continuous NaCl-containing aqueous films. Under higher magnification, Figs. 7b–d, both surfaces seem to exhibit an initial spreading area of the NaCl-droplet and also a secondary spreading area, similar to what has been reported before on both bare Zn [23,24] and bare Cu [12]. Both the initial and the secondary spreading areas are much more confined on HZ7 than on DP.

In the centre of the initial droplet area, elemental analysis of the corrosion products showed the presence of mainly Zn, Cl and O, while in the more peripheral, secondary, spreading area the main elements detected were Zn, C, O. Based on basic corrosion cell theory [25], one may expect a gradient both in potential and in chemical composition from the centre of the initial NaCl droplet area (anodic area with lower pH and higher chloride concentration) to the peripheral spreading area (cathodic area with higher local pH and lower chloride content). As a consequence of the radial distribution in potential and in local chemistry in the NaCl spreading area [24], and combined with the elemental analysis presented above, the formation of the commonly occurring compound simonkolleite, $Zn_5(OH)_8Cl_2\cdot H_2O$, is expected to be formed in the central anodic part, and hydrozincite, $Zn_5(CO_3)_2(OH)_6$, to be formed preferentially in the more peripheral cathodic part. This distribution of corrosion products is similar to that found by Cole et al. [26,27], who studied formation of corrosion products on pure zinc beneath a single NaCl-droplet.

The question if a hydrophobic surface is advantageous for obtaining a corrosion protective surface or not has been discussed before [10], and the answer depends on the actual corroding system studied. On one hand, poor initial surface wetting properties hinder the aqueous film to reach the metal surface. On the other hand, good wetting properties may disperse the aqueous film more efficiently and increase the evaporation rate of the film. To explore this question in some detail under current exposure conditions, IRAS was used to follow the growth of the corrosion product species in situ. A particular advantage is the ability of the technique to obtain semi-quantitative data [14], so that comparisons can be made of
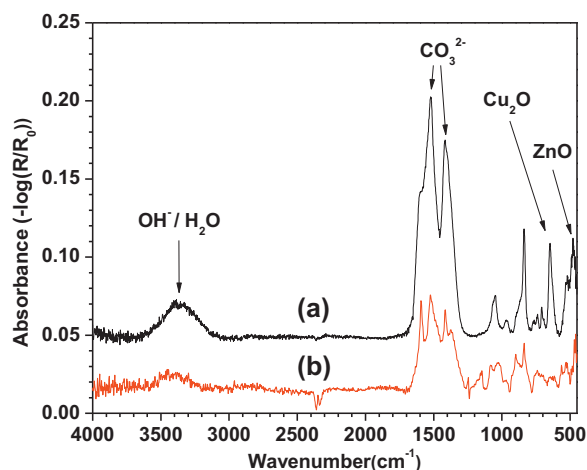
Fig. 8. In situ IRAS spectrum obtained on Cu40Zn (DP (a) and HZ7 (b)) exposed for 6 wet/dry cycles with pre-deposited NaCl ($4 \, \mu g \, cm^{-2}$).

the amount of species formed on the differently prepared Cu40Zn surfaces as a function of exposure time.

Fig. 8 displays the in situ IRAS spectra obtained for diamond polished Cu40Zn (DP) and Cu40Zn with pre-formed hydrozincite (HZ7), whereby both surfaces were subject to pre-deposited NaCl and subsequent exposure to 6 wet/dry cycles. The same four main species as in Fig. 3 were identified, all indicated by arrows, but with different amplitudes. From lower to higher wavenumbers: zincite (ZnO), cuprite (Cu_2O), CO_3^{2-} (from hydrozincite, $Zn_5(CO_3)_2(OH)_6$) and OH^-/H_2O. It should be remembered that the IRAS-data represent the overall composition of an area sized almost 10 mm and therefore cannot probe local variations in chemical composition. The IRAS set-up can furthermore not detect simonkolleite ($Zn_5(OH)_8Cl_2 \cdot H_2O$), because the specific wavenumber of the Zn–Cl vibrations are below the cutoff frequency of around $450 \, cm^{-1}$. However, as previously indicated by the SEM investigation and supported by literature findings, simonkolleite forms in the center of the initial droplet area.

Fig. 9 displays the growth of two of the main corrosion products that develop or form on the surface of Cu40Zn with time, hydrozincite (Fig. 9a) and Cu_2O (Fig. 9b). It should be remembered that both phases were present already from start of the exposure. The data is presented in absorbance units and allows comparisons to be made of the amounts of each species between the two Cu40Zn surfaces investigated, DP and HZ7. The tendency is very clear that the formation rates of both hydrozincite and cuprite are quite suppressed for Cu40Zn with preformed hydrozincite (HZ7) compared to the diamond polished surface (DP). In summary, without being able to consider the formation of simonkolleite, it can be concluded that an increased surface coverage of hydrozincite reduces the initial spreading ability of the NaCl-containing droplets and thereby lowers the overall formation rate of hydrozincite and cuprite.

3.4. Possible influence of microstructure on initial corrosion of Cu40Zn

Although the investigated Cu40Zn alloy contains two main phases with demonstrated variations in Volta potential along the surface, see previous Section 3.1, the results presented herein have so far not indicated any influence of alloy microstructure on the corrosion results. A possible reason may be that the NaCl-deposition of $4 \, \mu g \, cm^{-2}$ is too extensive for revealing any microstructural influence. For this reason two different amounts of predeposited NaCl, 0.1 and $4 \, \mu g \, cm^{-2}$, were applied on two Cu40Zn surfaces, DP and HZ7, and the results compared. Corrosion initation was primarily

analyzed by means of LOM and SEM/EDS for morphology and elemental compositional analyses, and confocal Raman spectroscopy (CRM) for lateral distribution of corrosion products formed.

Fig. 10a shows the morphology of the diamond polished Cu40Zn surface (pre-deposited with $0.1 \, \mu g \, cm^{-2}$ NaCl) exposed to 1 wet/dry cycle by means of LOM. A large circular darker area appears in the image, which indicates the interaction of a NaCl droplet with the surface upon deliquescence of deposited NaCl. The slightly zinc-richer β-phase inside the droplet area is seen as darker features compared with the surrounding α-matrix. CRM measurements were conducted on the square-sized area seen in Fig. 10a. The results reveal an enhanced formation of cuprite, Cu_2O (Fig. 10b, main peaks at 219, 424 and $636 \, cm^{-1}$) [9] and of zinc oxide, ZnO (Fig. 10c, main peaks at $426 \, cm^{-1}$, crystalline ZnO, and $560 \, cm^{-1}$, amorphous ZnO) [28] in the β-phase.

The microstructure evidently has a weak influence in which the slightly zinc-richer β-phase, of lower Volta potential compared with the surrounding α-phase matrix, has corroded faster with an initial formation of the corrosion products cuprite and zincite. Such microstructure effects, however, cannot be seen for the surface pre-deposited with the higher amount of NaCl ($4 \, \mu g \, cm^{-2}$) with no visible preference for either phase to corrode selectively.

It is also interesting to note that pre-formation of hydrozincite levels out the nobility differences between the α- and β-phases as revealed by SKPFM (not shown here) so that no microstructural effects can be seen, neither for $0.1 \, \mu g \, cm^{-2}$ nor for $4 \, \mu g \, cm^{-2}$ pre-deposited NaCl.

The results are in agreement with recent literature findings [17], in which similar microstructural effects between areas of slightly different Zn-content could be observed when a Cu20Zn alloy was exposed to a dilute NaCl solution. As a result of the relatively lower Volta potential, the zinc-richer phase initially corroded faster with zinc selectively released (dezincification) from this phase, and with concomitant preferential formation of cuprite and zincite at these positions. In agreement with the current study, such effects could not be seen in more concentrated NaCl-solutions.

3.5. Overall discussion

The starting point for this investigation has been the suppression or lack of corrosion product flaking in chloride-containing atmospheric environments previously observed for a few Cu–Zn alloys [9]. This was attributed to the formation of hydrozincite, $Zn_5(CO_3)_2(OH)_6$, and it was suggested that this corrosion product suppressed the interaction between the alloy surface and chlorides. However, the results permitted no real mechanistic evidence for the role of hydrozincite to be established.

Based on the experimental results presented herein we can now propose a possible mechanism for the influence of hydrozincite on initial corrosion of Cu40Zn in chloride-containing atmospheric environments, as schematically depicted in Fig. 11.

The diamond polished Cu40Zn surface consists mainly of cuprite (Cu_2O) and zincite (ZnO) and is characterized by a high wettability and low contact angle for pure water. When NaCl particles are pre-deposited on such a high energy surface and exposed to cyclic wet/dry exposure conditions with a relative humidity that exceeds the point of deliquescence for NaCl (approx. 75% at room temperature), the NaCl-containing droplets spread and an thin continous aqueous film containing sodium and chloride ions forms that covers most of the surface. At lower NaCl deposition load ($0.1 \, \mu g \, cm^{-2}$), a clear influence of the microstructure of the dual-phase alloy can be seen. The β-phase, having a lower Volta potential, is initially selectively corroded resulting in further formation of cuprite and zincite. However, at higher NaCl deposition load ($4 \, \mu g \, cm^{-2}$) no influence of alloy microstructure can be seen on the growth and distribution of corrosion effects. For comparison, a NaCl deposition rate of
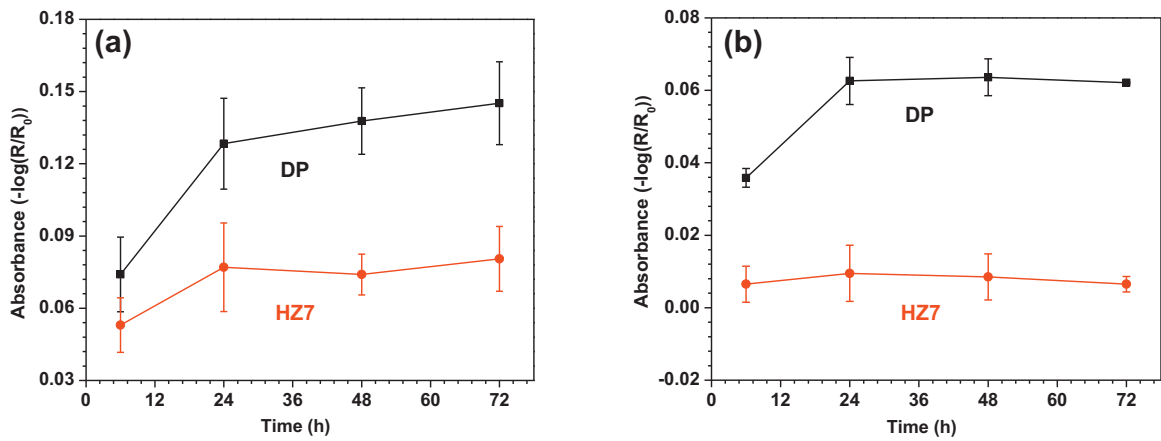
Fig. 9. Formation (in absorbance units) of main corrosion product species as a function of exposure time: (a) hydrozincite, (b) cuprite. The data has been generated for Cu40Zn (DP and HZ7) after pre-deposition of NaCl ($4\,\mu g\,cm^{-2}$ NaCl) and subsequent exposures to one (6 h), two (24 h), four (48 h) and six (72 h) wet/dry cycles respectively. The error bars are based on 2 independent measurements.
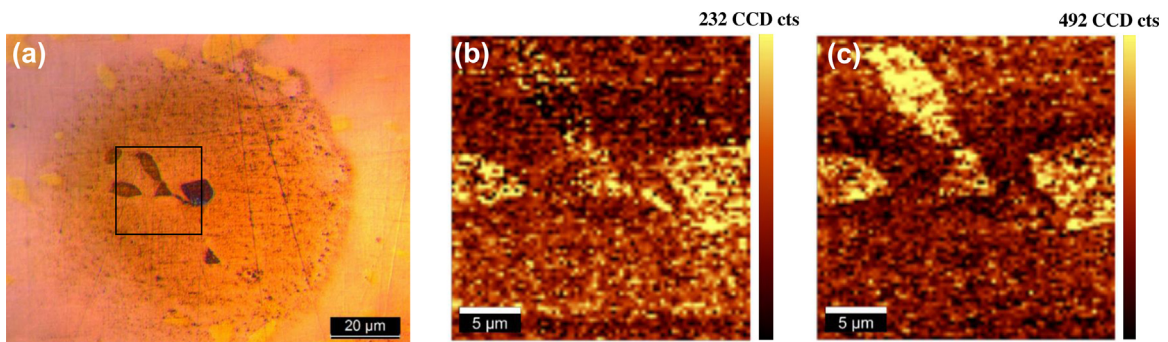

Fig. 10. Optical images (a) and combined Raman mapping images in the square area obtained with CRM on Cu_2O ((b), integrated between 150 and $250\,cm^{-1}$), ZnO ((c), integrated between 400 and $600\,cm^{-1}$) of corrosion products formed on Cu40Zn with pre-deposited NaCl ($0.1\,\mu g\,cm^{-2}$) exposed for 1 cycle at 90% RH.
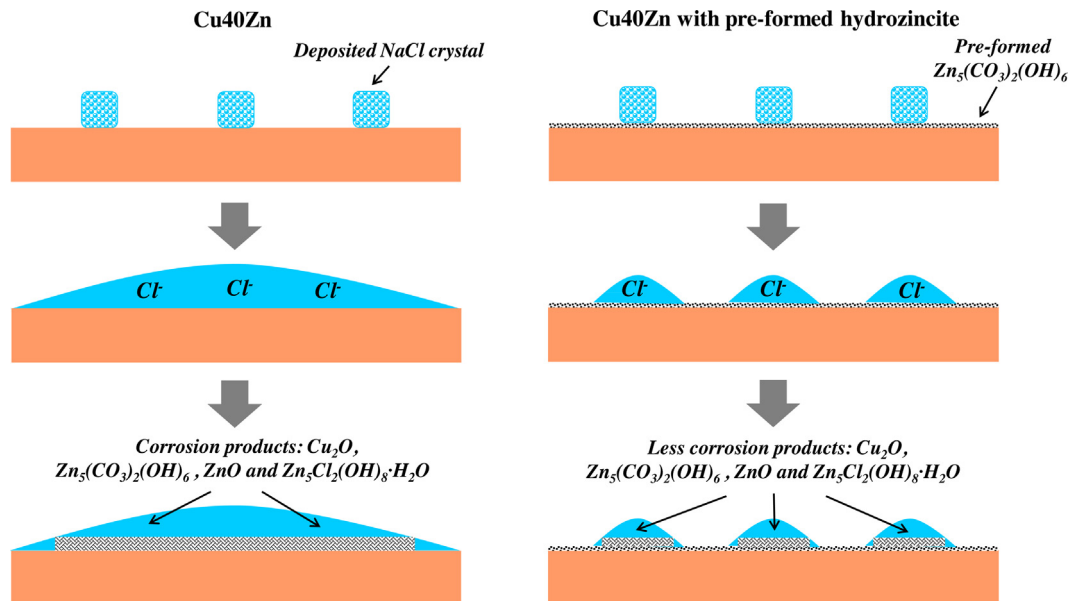

Fig. 11. Schematic illustration of the influence of hydrozincite on the initial corrosion of Cu40Zn.

$4\,\mu g\,cm^{-2}$ during three days of cyclic exposure conditions, can be compared with $13.3\,mg\,m^{-2}\,d^{-1}$, corresponding to salinity class S_1 according to the ISO classification 9223 [29].

When the Cu40Zn alloy was pre-treated to form hydrozincite as a major surface species, contact angle measurements of small water droplets showed that the surface wettability was largely reduced compared to the diamond polished surface. This wettability change has a major influence on the spreading of NaCl droplets on Cu40Zn. The more hydrophobic hydrozincite-dominating surface results in more confined and discrete NaCl droplets than a

diamond polished surface dominated by cuprite and zincite. Complementary surface roughness measurements with AFM and XPS supported that the influence of hydrozincite to reduce wettability and surface spreading mainly was due to surface chemistry effects rather than surface roughness and contamination effects. The limited spreading of NaCl droplets caused by pre-formed hydrozincite results in a more confined initial spreading of corrosion effects on the hydrophobic Cu40Zn surface than on the more hydrophilic, diamond polished, Cu40Zn surface. IRAS furthermore showed that the growth of two of the three dominating corrosion products, hydrozincite and cuprite, was significantly lower on the hydrophobic surface with preformed hydrozincite. Efforts were also made to remove the corrosion products after exposure and analyze the depth and extent of corrosion attacks. Although these observations were without any quantitative precision, they suggest a substantial reduction in corrosion attack of Cu40Zn with pre-formed hydrozincite. Hence, hydrozincite clearly protects the Cu40Zn surface from corrosion under present exposure conditions. Although schematically depicted as a uniform layer in Fig. 11, there is no clear evidence of a uniform layer of hydrozincite from the experimental data.

Comparing the conclusions obtained with those from others, a previous experimental study has shown that synthetic zinc hydroxycarbonate and zinc oxide are more hydrophobic and less porous compared to synthetic zinc hydroxychloride and zinc hydroxysulphate [10]. The preparation of hydrozincite in that study was completely different from here. The protection of hydrophobic surfaces against corrosion initiation has been investigated elsewhere, showing that surfaces with reduced wettability could hinder corrosion due to reduced attraction between the saline solution and the substrate [30,31]. A corrosion protective effect of hydrozincite has been reported previously and found to be more efficient than those of other basic zinc compounds [23]. This has been attributed to a negatively charged surface of hydrozincite below the isoelectric point of pH 6, resulting in the repulsion of chloride ions and the concomitant prevention of chloride-induced atmospheric corrosion [32]. Other studies suggest that hydrophobic surfaces not always are advantageous for improving the corrosion resistance [10,33]. It has also been reported for long-term field exposure conditions that the corrosion rate of zinc decreases due to the promotion of simonkolleite formation preventing carbonate formation at pH below 8 [34]. However, these reported conclusions have been obtained at quite different exposure conditions and may not contradict our conclusion of the role of hydrozincite for improving the corrosion protection of Cu40Zn exposed to the current chloride-containing laboratory exposure.

4. Conclusions

In a previously proposed model for corrosion product flaking of Cu-based alloys in chloride-containing atmospheres, hydrozincite, $Zn_5(CO_3)_2(OH)_6$, was suggested to suppress the interaction between the alloy surface and chlorides.

Surface formation of hydrozincite could be produced by exposure of diamond polished Cu40Zn to air at 70% relative humidity and with addition of 1000 ppm of CO_2. Besides hydrozincite, smaller amounts of cuprite, Cu_2O, and zinc oxide, ZnO were also detected.

The presence of hydrozincite results in a decreased initial surface wettability of Cu40Zn, as judged from water contact angle measurements. This reduces the initial spreading ability of the NaCl-containing droplets and lowers the initial corrosion rate when the alloy is exposed to pre-deposited NaCl and wet/dry cycles.

At lower amount of predeposited NaCl ($0.1\,\mu g\,cm^{-2}$) a clear influence of the microstructure of the dual-phase alloy can be seen with initial selective corrosion of the less noble β-phase of higher zinc content. The influence of microstructure could not be discerned either for surfaces pre-formed with hydrozincite, or for higher amounts of pre-deposited NaCl ($4\,\mu g\,cm^{-2}$).

References

[1] Copper Development Association, A guide to working with copper and copper alloys.

[2] G.F. Vander Voort (Ed.), ASM Handbook: Metallography and Microstructures, ASM International, 2004.

[3] A. Krätschmer, I. Odnevall Wallinder, C. Leygraf, The evolution of outdoor copper patina, Corros. Sci. 44 (2002) 425–450.

[4] I. Odnevall Wallinder, X. Zhang, S. Goidanich, N. Le Bozec, G. Herting, C. Leygraf, Corrosion and runoff rates of Cu and three Cu-alloys in marine environments with increasing chloride deposition rate, Sci. Total Environ. 472 (2014) 681–694.

[5] D. de la Fuente, J. Simancas, M. Morcillo, Morphological study of 16-year patinas formed on copper in a wide range of atmospheric exposures, Corros. Sci. 50 (2008) 268–285.

[6] H. Strandberg, L.G. Johansson, Some aspects of the atmospheric corrosion of copper in the presence of sodium chloride, J. Electrochem. Soc. 145 (1998) 1093–1100.

[7] Z.Y. Chen, D. Persson, F. Samie, S. Zakipour, C. Leygraf, Effect of carbon dioxide on sodium chloride-induced atmospheric corrosion of copper, J. Electrochem. Soc. 152 (2005) B502–B511.

[8] S. Goidanich, J. Brunk, G. Herting, M.A. Arenas, I. Odnevall Wallinder, Atmospheric corrosion of brass in outdoor applications: patina evolution, metal release and aesthetic appearance at urban exposure conditions, Sci. Total Environ. 412–413 (2011) 46–57.

[9] X. Zhang, I. Odnevall Wallinder, C. Leygraf, Mechanistic studies of corrosion product flaking on copper and copper-based alloys in marine environments, Corros. Sci. 85 (2014) 15–25.

[10] T.H. Muster, A.K. Neufeld, I.S. Cole, The protective nature of passivation films on zinc: wetting and surface energy, Corros. Sci. 46 (2004) 2337–2354.

[11] X. Zhang, C. Leygraf, I. Odnevall Wallinder, Atmospheric corrosion of Galfan coatings on steel in chloride-rich environments, Corros. Sci. 73 (2013) 62–71.

[12] Z.Y. Chen, S. Zakipour, D. Persson, C. Leygraf, Effect of sodium chloride particles on the atmospheric corrosion of pure copper, Corrosion 60 (2004) 479–491.

[13] H. Gil, C. Leygraf, Quantitative in situ analysis of initial atmospheric corrosion of copper induced by acetic acid, J. Electrochem. Soc. 154 (2007) C272–C278.

[14] T. Aastrup, C. Leygraf, Simultaneous infrared reflection absorption spectroscopy and quartz crystal microbalance measurements for in situ studies of the metal/atmosphere interface, J. Electrochem. Soc. 144 (1997) 2986–2990.

[15] G. Pantazopoulos, A. Vazdirvanidis, Characterization of the microstructural aspects of machinable α-β phase brass, Microsci. Anal. 22 (2008) 13–16.

[16] J. Dutkiewicz, F. Masdeu, P. Malczewski, A. Kukula, Microstructure and properties of α + β brass after ECAP processing, Arch. Mater. Sci. Eng. 39 (2009) 80–83.

[17] M. Forslund, C. Leygraf, C. Lin, J. Pan, Radial spreading of localized corrosion-induced selective leaching on alpha-brass in dilute NaCl solution, Corrosion 69 (2013) 468–476.

[18] P. Qiu, C. Leygraf, I. Odnevall Wallinder, Evolution of corrosion products and metal release from Galvalume coatings on steel during short and long-term atmospheric exposures, Mater. Chem. Phys. 133 (2012) 419–428.

[19] M. Forslund, C. Leygraf, P.M. Claesson, C.J. Lin, J.S. Pan, Micro-galvanic corrosion effects on patterned copper-zinc samples during exposure in humidified air containing formic acid, J. Electrochem. Soc. 160 (2013) C423–C431.

[20] A.K. Neufeld, I.S. Cole, Using Fourier transform infrared analysis to detect corrosion products on the surface of metals exposed to atmospheric conditions, Corrosion 53 (1997) 788–799.

[21] J. Duchoslav, M. Arndt, T. Keppert, G. Luckeneder, D. Stifter, XPS investigation on the surface chemistry of corrosion products on ZnMgAl-coated steel, Anal. Bioanal. Chem. 405 (2013) 7133–7144.

[22] M. Mantel, J.P. Wightman, Influence of the surface chemistry on the wettability of stainless steel, Surf. Interface Anal. 21 (1994) 595–605.

[23] I.S. Cole, N.S. Azmat, A. Kanta, M. Venkatraman, What really controls the atmospheric corrosion of zinc? Effect of marine aerosols on atmospheric corrosion of zinc, Int. Mater. Rev. 54 (2009) 117–133.

[24] A.K. Neufeld, I.S. Cole, A.M. Bond, S.A. Furman, The initiation mechanism of corrosion of zinc by sodium chloride particle deposition, Corros. Sci. 44 (2002) 555–572.

[25] D. Landolt, Introduction to surface reactions: electrochemical basis of corrosion, in: J.O.P. Marcus (Ed.), Corrosion Mechanisms in Theory and Practice, Marcel Dekker, Inc., New York, 1995, pp. 1–18.

[26] I.S. Cole, T.H. Muster, S.A. Furman, N. Wright, A. Bradbury, Products formed during the interaction of seawater droplets with zinc surfaces: I. Results from 1- and 2.5-day exposures, J. Electrochem. Soc. 155 (2008) C244–C255.

[27] I.S. Cole, T.H. Muster, D. Lau, N. Wright, N.S. Azmat, Products formed during the interaction of seawater droplets with zinc surfaces: II. Results from short exposures, J. Electrochem. Soc. 157 (2010) C213–C222.

[28] J. Hedberg, N. Le Bozec, I. Odnevall Wallinder, Spatial distribution and formation of corrosion products in relation to zinc release for zinc sheet and coated pre-weathered zinc at an urban and a marine atmospheric condition, Mater. Corros. (2011) 1–9.

[29] ISO 9223, Corrosion of metals and alloys—Corrosivity of atmospheres—Classification determination and estimation (2012).

[30] H. Cho, J. Lee, S. Lee, W. Hwang, Durable superhydrophilic/phobic surfaces based on green patina with corrosion resistance, Phys. Chem. Chem. Phys. 17 (2015) 6786–6793.

[31] P. Wang, D. Zhang, Z. Lu, Advantage of super-hydrophobic surface as a barrier against atmospheric corrosion induced by salt deliquescence, Corros. Sci. 90 (2015) 23–32.

[32] T.H. Muster, I.S. Cole, The protective nature of passivation films on zinc: surface charge, Corros. Sci. 46 (2004) 2319–2335.

[33] T.H. Muster, A. Bradbury, A. Trinchi, I.S. Cole, T. Markley, D. Lau, S. Dligatch, A. Bendavid, P. Martin, The atmospheric corrosion of zinc: the effects of salt concentration, droplet size and droplet shape, Electrochim. Acta 56 (2011) 1866–1873.

[34] T. Prosek, D. Thierry, C. Taxén, J. Maixner, Effect of cations on corrosion of zinc and carbon steel covered with chloride deposits under atmospheric conditions, Corros. Sci. 49 (2007) 2676–2693.